Trans-layer and inter-layer fracture behavior of extrusion-based 3D printed concrete under three-point bending

Yuxiang Tang[a], Jianzhuang Xiao[a,b,*], Tao Ding[a], Haoran Liu[a], Mingzhong Zhang[c]

[a] *School of Traffic and Transportation Engineering, Changsha University of Science & Technology, Changsha 410114, China*

[b] *Department of Structural Engineering, College of Civil Engineering, Tongji University, Shanghai 200092, China*

[c] *College of Civil Engineering and Architecture, Guangxi University, Nanning 530004, China*

[d] *Department of Civil, Environmental and Geomatic Engineering, University College London, London WC1E 6BT, UK*

Abstract: This paper presents a systematic study on the effect of layer-by-layer printing process on the fracture behavior of hardened extrusion-based 3D printed concrete (3DPC). Based on three-point bending tests on center-notched beams, the fracture response of printed specimens with two fracture patterns including crack propagation across layers (trans-layer fracture) and crack propagation along layers (inter-layer fracture) was compared with that of cast specimens. The fracture mechanism of 3DPC was explored using the fracture parameters and fracture process zone (FPZ) characteristics. Experimental phenomena can be explained by the additional interlaminar cracking in FPZ of concrete introduced by the layer-by-layer stacking process. It could produce a toughening effect if cracks propagate through layers, as it is beneficial to reduce stress concentration and improve deformability. In the printing process design of 3DPC, such feature can be rationally utilized to transform the process-induced weak interfaces from inherent defects to toughening means.

Keywords: 3D concrete printing; Layer orientation; Fracture behavior; Fracture process zone; Interlaminar cracking; Toughening mechanism

* Corresponding author. E-mail address: jzxiao@gxu.edu.cn; jzx@tongji.edu.cn (J. Xiao)

Nomenclature

L	length of beam
D	depth of beam
t	thickness of beam
S	span of beam
a_0	initial crack length
α_0	ratio of initial crack length to beam depth
ε_{xx}	strain in x direction which is horizontal
P_{ini}	initial cracking load
P_c	peak load
$CMOD_c$	critical crack mouth opening displacement at peak load
$CTOD_c$	critical crack tip opening displacement at peak load
$CTOD_c^{TP}$ and $CTOD_c^{DK}$	$CTOD_c$ calculated from two-parameters fracture model (TPFM) and double-K fracture model (DKFM)
a_c	critical effective crack length
a_c^{TP} and a_c^{DK}	critical effective crack length calculated from TPFM and DKFM
Δa	crack growth length
E_c	Young's modulus
E_c^{TP} and E_c^{DK}	Young's modulus calculated from TPFM and DKFM
h_0	thickness of the holder for clip gauge
w_{FPZ}	width of fracture process zone
m	mass of beam between the supports
W_0	area under the load–deflection curve
δ_0	deflection at final failure
G_f	fracture energy
K_{Ic}^{ini}	initial fracture toughness
K_{Ic}^{un}	unstable fracture toughness
X, Y and Z	directions of printing filament
x and y	directions of measuring surface
u and v	displacements in x and y direction

1. Introduction

Over the past decade, the additive manufacturing (AM) technology has received worldwide attention and developed rapidly for construction industry [1, 2]. As an emerging AM technology, 3D concrete printing brings both opportunities and challenges to the digital fabrication in construction [3, 4]. It has many advantages over conventional construction methods in terms of construction period, cost, quality, and flexibility [5]. For instance, automated construction improves productivity and safety; personalized customization makes complex structural shapes possible; and high construction accuracy reduces material waste [6]. The extrusion-based layer-by-layer printing process imposes new specific requirements on concrete as ink material (called 3D printed concrete, 3DPC) such as mix design optimization [7], fresh state control [8], and hardening performance evolution [9]. Regarding mix design and fresh state of 3DPC, the primary purpose is to satisfy pumpability, extrudability, and buildability, which are essential process-related material properties needed for successful 3D concrete printing [10]. As such, it is particularly important to strictly control the rheology performance of materials and to rationally characterize it using different parameters [11], including static yield stress, penetration resistance, green strength, and slump. Apart from the printability of 3DPC, the bond strength between layers is also important for achieving the target strength and durability of hardened concrete [7].

In recent years, the interfacial bond properties between layered filaments of hardened 3DPC have been increasingly studied. It was reported that the interlayer interval time has a pronounced influence on the bond strength between layers in three perpendicular directions [12]. Sanjayan *et al.* [13] found that the weak interlaminar strength is closely associated with the surface moisture content at the layer interface, as the water loss is confined to the dry area at the free surface, causing incomplete cement hydration and more localized porosity [14]. By using X-ray computed tomography to visualize and quantify pore structures of 3DPC, Kruger *et al.* [15] observed the tri-axial spheroid shaped air voids which were elongated and flattened after extrusion and deposition of filaments. The effect of pore structure on 3DPC with coarse aggregates was explored by Liu *et al.* [16], who established the relationship between pore defect geometry and cracking damage. The enhanced interlocking (macro roughness) of the layer interface is an effective way to improve interlayer bonding strength [17, 18]. However, the adhesion between two adjacent process-induced layers of 3DPC is weaker than the cohesion of cast concrete [19]. As the layered structure of printed concrete may lead to higher degrees of anisotropy and inhomogeneity compared to traditional cast concrete [9], more focuses have been placed on the mechanical properties of hardened 3DPC under different loading directions. It was indicated that 3DPC exhibited significant anisotropy in compressive, splitting tensile, flexural, and shear strengths [20], affected by raw materials [21, 22] and printing parameters [12], but regardless of curing condition [23] and temperature [24] after forming. Xiao *et al.* [25] performed finite element

analysis on the mechanical behavior of 3DPC under compression and bending based on the traction-separation law and found that the quantity and strength of interfaces between printed filaments lead to changes in the anisotropic behavior of 3DPC.

Besides basic strength properties, it is also vital to study the fracture behavior of 3DPC, which is crucial for the safety design and durability assessment of concrete structures [26]. For 3DPC, the lack of fusion between layers can serve as an entry route for corrosion pollutants, leading to deterioration of concrete durability compared with the cast concrete [27]. Relatively few studies have been conducted on the load-induced fracture response of 3DPC. Nair *et al.* [22] explored the effect of printing layer height on fracture properties of plain and fiber-reinforced 3D-printed beams and found that smaller layer height was beneficial even though it induced more interfaces and longer printing time. Heever *et al*. [28, 29] numerically studied the fracture behavior of 3DPC beams under four-point bending based on the measured mechanical parameters. Yang *et al.* [30] proposed an analytical model to predict the tensile strength and fracture toughness of 3DPC loaded in different directions. These studies all indicate that the fracture behavior of 3DPC is obviously different from that of cast-in-mold concrete.

Due to the existence of weak interfaces introduced by the layer-by-layer printing process, most studies [12, 16, 31] show that hardened concrete typically has lower strength, *e.g.*, compressive, tensile, and flexural strengths, while the flexural strength of printed specimens is higher than that of cast ones. For instance, the flexural strength of 3DPC was found to be much higher than cast concrete when the loading direction was perpendicular to the extruded filaments [32]. This can be explained by the fact that casting relatively viscous 3D printable concrete may lead to high entrained and entrapped air content, while fiber alignment in the printing direction may increase 3DPC trans-interfacial flexural resistance by the increased energy consumption. The improved flexural properties were also observed for geopolymer [33], recycled concrete [21], and ultra-high ductile concrete [34], which can be ascribed to the layer-by-layer stacking process. The porous interlayers induced by the printing process can introduce more holes and voids (*i.e.*, initial defects) in hardened concrete [16, 23, 35]. How these initial defects evolve and develop in the layered structure of 3DPC until failure and thus determines the load bearing and deformation capacity of the material. To date, limited studies have explored the fracture properties of 3DPC to accurately distinguish various fracture types. For layer-by-layer 3DPC, the layer orientation obviously affects the crack propagation process. Most studies on fracture properties of 3DPC were mainly focused on fiber-reinforced concrete [22, 28-30], indicating that the existence of fibers affects the judgment of the fracture mechanism affected by the printing process to a certain extent.

The main purpose of this study is to systematically investigate the effect of layer-by-layer printing process on the fracture behavior of hardened plain concrete. Two fracture patterns of the printed

specimens were mainly considered, including cracks propagating across layers (namely trans-layer fracture) and cracks propagating along layers (namely inter-layer fracture). Three-point bending tests were performed on center-notched beams. Besides, it is necessary to monitor the crack development of materials with high accuracy and resolution during loading process. Digital image correlation (DIC) technique that has been widely adopted as an optical image measuring technique to study the fracture property of concrete materials [22, 36-39] was employed to capture the full-field deformation in this study. Based on the obtained fracture parameters and fracture process zone characteristics, the fracture failure mechanism of 3DPC was analyzed and discussed in depth, which could help optimize and guide the design of future 3D concrete printing process.

2. Experimental program

2.1 Materials

Ordinary Portland cement with grade of 42.5 was used as binder and river sand with particle size smaller than 2.36 mm was adopted as fine aggregate. The particle size distribution of cement and sand is presented in

Fig. 1. The fineness modulus and apparent density of sand were 2.44 and 2586 kg/m^3, respectively. The water-to-cement (w/c) ratio and sand-to-cement ratio were 0.35 and 1.00, respectively. To ensure the extrudability, buildability, workability, and open time of 3DPC, additional components including nano-clay, superplasticizer (powdered form), hydroxy propyl methyl cellulose (HPMC) and sodium gluconate (SG) were required to tailor the mix proportion [21, 40]. The specific mix proportion for 3DPC is listed in Table 1. The fluidity of the fresh mixture characterized using flow table test was found to be about 165 mm. As per the standard [41], the 28 d flexural strength and compressive strength of the hardened specimens with size of 160 × 40 × 40 mm^3 were found to be 4.9 ± 0.19 MPa and 50.6 ± 1.59 MPa, respectively.

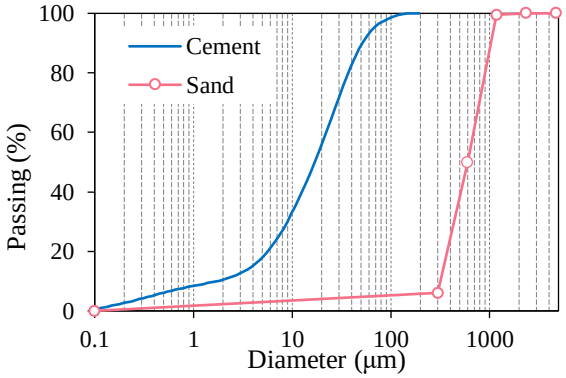

Fig. 1 Particle size distribution of cement and sand.

Table 1 Mix proportion of the printable mixture (kg/m^3).

Cement	Sand	Water	Nano-clay	Superplasticizer	HPMC	SG
1000	1000	350	5	1.52	1.28	0.7

2.2 3D printing and specimen details

As illustrated in Fig. 2a, a high-precision gantry printer with 1 m^3 printing area for mixture extrusion was employed to print specimens. For this printer, the horizontal printing plane and the vertical direction were defined as the X–Y plane and Z-axis, respectively. The printhead was equipped with a vertical auger-type screw and a circular nozzle with a diameter of 20 mm to extrude the material continuously and smoothly. During the printing process, the extrusion speed and the horizontal printing speed were set as 2.5 rad/s and 20 mm/s, respectively. Since the bond between layers can be increased under the contact stress when the nozzle size exceeded the printing height [42], the dimension of the extruded filament was controlled to be 20 mm and 10 mm in width and height, respectively. The print path was presented in Fig. 2b. The freshly printed specimen was left in place to avoid any disturbance, and covered with plastic film to maintain a sufficiently humid environment [43]. To compare the influence of construction methods, the mold was also used for casting at the same time. After 24 h, the specimen was transferred to saturated calcium hydroxide solution for curing of another 27 d to prevent leaching of calcium hydroxide from the specimens, which would affect the hydration process of cement and thus the concrete strength [44, 45].

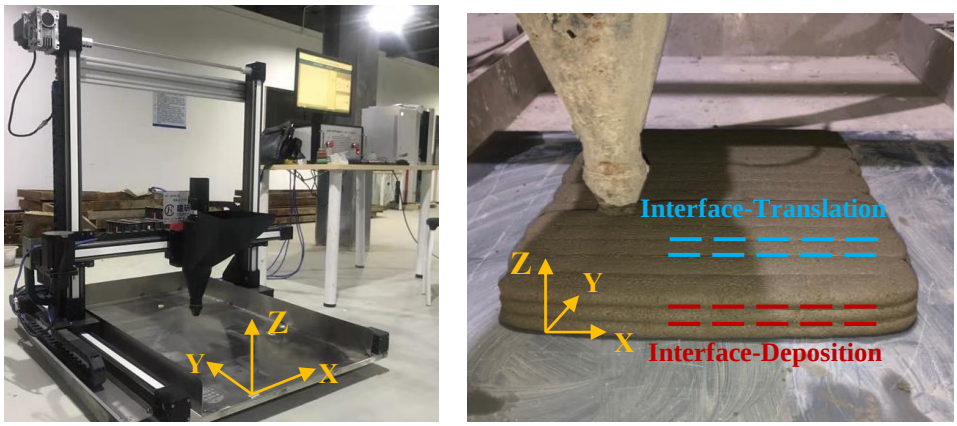

(a) Printer (b) Printing slab

Fig. 2 3D concrete printer and printed slab.

To investigate the anisotropic fracture behavior of 3DPC, it is necessary to define a coordinate system first. Referring the actual printing process, the X-axis was the direction parallel to the printed filament, while the Y- and Z-axis was the direction perpendicular to the printed filament in the horizontal plane and the direction along the printing height, respectively. As seen in Fig. 3, the test specimens were divided into three types, including one cast-in-mold type (denoted as Group Cast) and two printed types. In this fracture test, based on the position of the initial notch (reflecting the main direction of crack propagation), the printed types were divided into crack propagating through the layers (trans-layer fracture) and crack propagating along the layers (inter-layer fracture). Generally, there are two main types of interface for the 3D printed specimen [25], as displayed in Fig. 2b and Fig. 3. One is that when the layered filaments are deposited along Z-axis, the interface between filaments on the plane of X-axis and Y-axis, namely Interface-Deposition. The other is that when the

printing filament is translated along Y-axis, the interface between filaments on the plane of X-axis and Z-axis, namely Interface-Translation. The trans-layer fracture type included two groups: crack propagates through the translation interface and the deposition interface, denoted as Group Trans-D and Group Trans-T. The inter-layer fracture type also included two groups: crack propagates along the translation interface and the deposition interface, denoted as Groups Inter-D and Group Inter-T. A total of five groups of specimens were tested in this study. The details of layer and loading orientations for the specimens are depicted in Fig. 3.

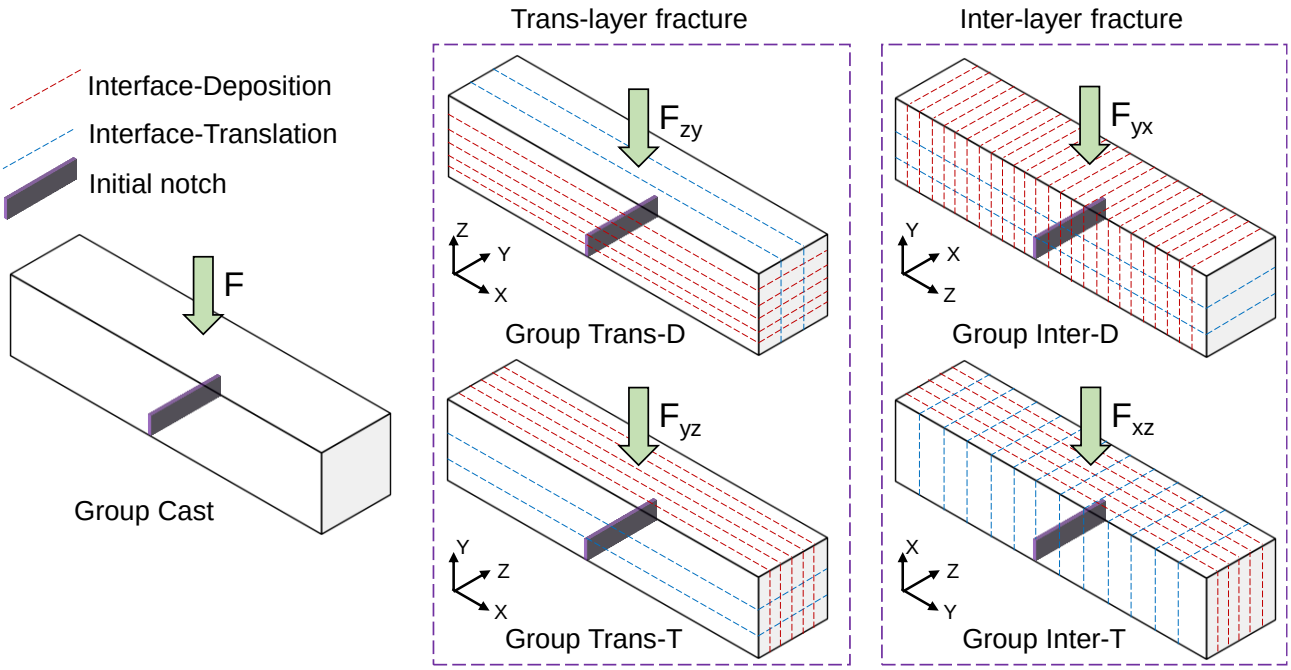

Fig. 3 Layer and loading orientations for the test specimens (*Notes:* F_{ab}, a and b denote the directions of loading and initial notch thickness, respectively).

The dimension of the test specimens was designed as 280 mm × 60 mm × 60 mm (length × depth × thickness), mainly to ensure there were at least three filaments (*i.e.*, two interfaces) in any direction [9] and the span-depth ratio was equal to 4 referring to RILEM recommendations [46]. The specimens of Group Cast were directly cast by using customized molds and compacted by employing a vibrating table. The specimens of Groups Trans-D, Trans-T and Inter-T were cut from the printed slabs with the dimension of 260 mm × 320 mm × 60 mm (X × Y × Z) after curing for 28 d, as shown in Fig. 2b. The specimens of Group Inter-D were cut from a printed prism with size of 300 mm × 60 mm × 280 mm (X × Y × Z). Each group consisted of four test specimens. A saw-cut notch with the dimension of 20 mm × 3 mm (depth × width) was made for each specimen. The initial notch-to-depth ratio was equal to 1/3 according to RILEM recommendations [46].

2.3 Testing method

Three-point bending tests on notched beam were performed using an MTS electronic universal testing machine (CMT5505), as illustrated in Fig. 4a. The specimen was placed on two bottom rollers with

distance of 240 mm. To determine the crack mouth opening displacement (CMOD), a clip gauge (YYJ-2/5) was installed at the bottom of the beam by two adhered steel sheets with thickness of 1.5 mm (Fig. 4b). Two linear variable differential transformers (LVDTs) were used to measure the mid-span deflection (δ). To estimate the initial cracking load, two strain gauges with distance of 20 mm were attached symmetrically on the polished surface near the notch tip as per RILEM standard [47].

An industrial camera was utilized to capture the surface images with an interval of 1 s, and the DIC technology was employed to obtain the deformation during the loading process. Specifically, the deformation of specimens can be obtained by comparing the reference and deformed images before and after loading. In post-processing of digital images, an adjustable square region of the reference and deformed images are defined as the reference subset and the target subset, respectively. The displacement can be calculated by tracking the spatial change of gray value between the reference subset and the deformed subset. Besides the subset size, the step size (*i.e.*, the distance between subsets) is also a necessary setting parameter which would affect the calculation results. To apply this technique, speckles were generated on the observing area first. Specifically, after polishing and cleaning the surface, the white paint was evenly sprayed to make a white background, and then the black paint was randomly sprayed to generate well-distributed black spots (see Fig. 4a). The speckle size was about 5 pixels, and the scale of the measurement was about 10 pixel/mm. A subset size of 21 pixels and step size of 13 pixels was adopted. More details about the employment and post-treatment for DIC technique can be found in Ref. [48].

After confirming that all measuring and acquisition equipment was prepared well, the specimen was first preloaded with a load of 50 N to reduce the effect of possible loosening and obtain the reliable data. To achieve quasi-static loading for observation of stable crack propagation, the loading is usually controlled by *CMOD*. Given that the requirement of loading control is that the recorded displacement information is complete and stable, the load-line deflection control is also acceptable as per RILEM recommendations [46]. Thus, the fracture test was conducted at a constant loading rate of 0.03 mm/min using the displacement control of the loading point (*i.e.*, the displacement of the MTS crosshead), which was determined by some preliminary experiments. At this loading rate, the peak load was reached at about 3-5 min and the whole loading process was about 10-15 min. The applied load and *CMOD* were collected by the MTS machine itself while the data of δ and strain gauges was recorded using a static strain tester (DH3818Y). To obtain more reliable results, specimens in one group were loaded within one day without interruption.

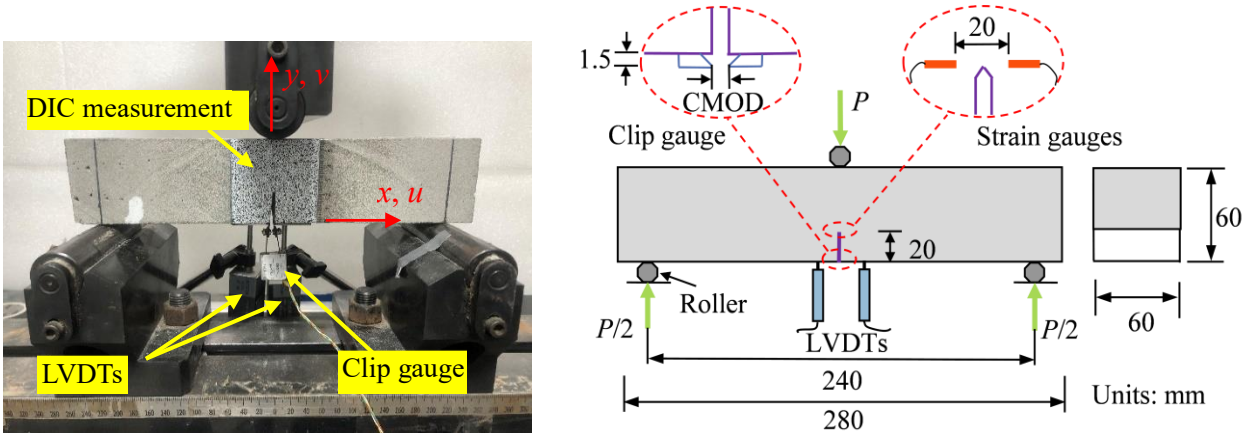

(a) Photo (front view) (b) Diagrammatic sketch (rear view)

Fig. 4 Three-point bending test setup.

3. Experimental results

The experimental results of all groups are presented and analyzed in this section, including load-displacement curves, crack growing and opening, fracture process zone, fracture energy, and double-*K* fracture parameters. The specific fracture parameters of 3DPC specimens are summarized in Table 2. Generally, the results of concrete fracture tests exhibit a large scatter due to the heterogeneity of the material itself, the sensitivity of the specimen notch, and the strictness of the loading setup [49]. Thus, as per RILEM recommendations [46], four specimens were tested for each group, and the average values of three closest specimens were adopted for further analysis. Given the result scatter, the closest three of the four specimens were selected in this study. The error bars in subsequent figures represent one standard deviation (SD) of experimental results obtained from three replicate specimens.

3.1. Load-CMOD curves

Fig. 5 shows the load *P-CMOD* curves of mold-cast and 3D-printed specimens, including individual curves and typical curves (*i.e.*, the middle curve based on the peak load), indicating that the construction method has a limited effect on the shape of curves. The relationship between *P* and *CMOD* of all groups can be basically divided into three stages. For better observation, a typical specimen was taken as an example and its result is depicted in Fig. 6. At the early loading stage, the specimen is nearly in linear elastic deformation and the strain at the notch tip increases with the increasing load. With the initiation of cracking, nonlinear deformation begins to appear, and the strain reaches its maximum value. The load at this time (about 504 N) can be considered as the crack initiation load (P_{ini}). Then, the increasing slope of *CMOD* declines gradually with the increase of load, indicating that the nonlinear deformation rises, and the crack is in the stage of stable propagation. The strain of concrete near the notch tip drops continuously due to the release of strain energy after initial cracking. At peak load, the strain energy accumulated in the previous stage is released rapidly and the crack propagates unsteadily, which is reflected in the sharply falling portion of the curve.

Table 2 Experimental results of all groups.

Group	No.	ρ (kg.m^{-3})	P_{ini} (N)	P_c (N)	$CMOD_c$ (mm)	$CTOD_c$ (mm)	a_c (mm)	w_{FPZ} (mm)	E_c^{TP} (GPa)	E_c^{DK} (GPa)	G_f (N/m)	K_{Ic}^{ini} (MPa.m$^{1/2}$)	K_{Ic}^{un} (MPa.m$^{1/2}$)
Cast	1	2156	669	1163	0.040	0.015	34.0	3.3	22.9	22.7	100.0	0.384	1.121
	2	2198	504	935	0.054	0.030	40.0	3.2	22.3	21.7	93.5	0.269	1.210
	3	2096	557	967	0.035	0.016	31.3	3.1	23.3	22.8	84.9	0.297	0.956
	Mean	2150	577	1022	0.043	0.020	35.1	3.2	22.8	22.4	92.8	0.317	1.096
	SD	51	84	124	0.010	0.008	4.5	0.1	0.5	0.6	7.6	0.060	0.129
Trans-D	1	2165	559	1148	0.075	0.044	37.7	4.0	20.4	19.6	164.0	0.283	1.493
	2	2138	646	1331	0.052	0.025	34.1	4.4	20.3	19.5	122.5	0.338	1.250
	3	2105	594	1244	0.073	0.042	37.1	4.3	20.8	20.0	155.0	0.292	1.542
	Mean	2136	600	1241	0.067	0.037	36.3	4.2	20.5	19.7	159.5	0.304	1.428
	SD	30	44	91	0.013	0.010	1.9	0.2	0.3	0.3	6.3	0.029	0.156
Trans-T	1	2143	700	1517	0.066	0.031	35.7	4.6	20.1	19.9	188.4	0.372	1.564
	2	2108	567	1273	0.073	0.036	38.0	4.3	20.5	20.0	165.1	0.276	1.540
	3	2161	658	1390	0.067	0.034	37.1	4.5	20.1	19.9	182.5	0.339	1.535
	Mean	2137	642	1393	0.069	0.034	36.9	4.5	20.2	19.9	178.7	0.329	1.546
	SD	37	68	122	0.004	0.003	1.2	0.2	0.2	0.0	12.1	0.049	0.016
Inter-D	1	2109	358	635	0.042	0.022	36.1	2.4	20.3	19.8	66.4	0.193	0.860
	2	2048	370	642	0.046	0.025	41.4	2.6	22.0	21.1	45.9	0.324	0.953
	3	2143	400	708	0.042	0.019	37.9	2.7	18.1	17.3	54.4	0.214	0.795
	Mean	2100	376	661	0.043	0.022	38.5	2.6	20.1	19.4	55.6	0.244	0.869
	SD	48	22	40	0.002	0.003	2.7	0.2	2.0	1.9	10.3	0.070	0.080
Inter-T	1	2099	402	773	0.034	0.014	33.1	2.8	19.1	19.2	71.4	0.218	0.774
	2	2115	548	950	0.030	0.015	34.6	2.5	22.5	21.2	57.0	0.280	0.731
	3	2128	488	887	0.035	0.016	34.4	2.3	22.8	23.0	70.7	0.247	0.943
	Mean	2114	479	870	0.033	0.015	34.0	2.5	21.4	21.1	66.4	0.249	0.816
	SD	15	73	90	0.003	0.001	0.8	0.3	2.1	1.9	8.1	0.031	0.112

Notes: SD is the standard deviation. The G_f of Trans-D-2 was not adopted in this study because the difference with the average value of other test pieces was greater than 15%.

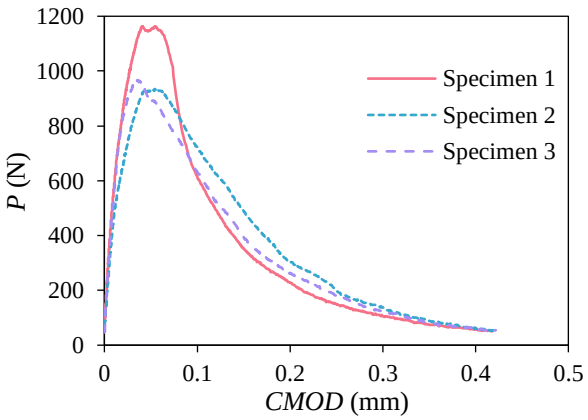

(a) Group Cast

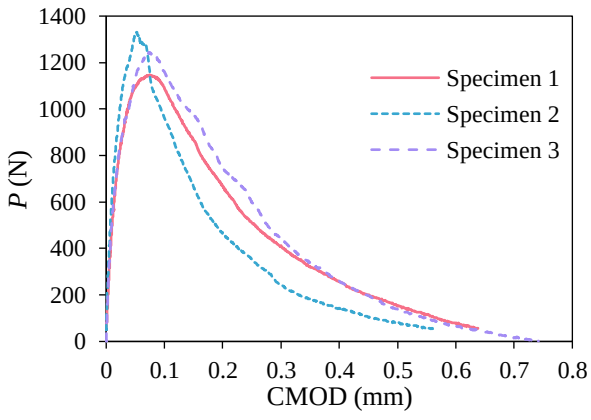

(b) Group Trans-D

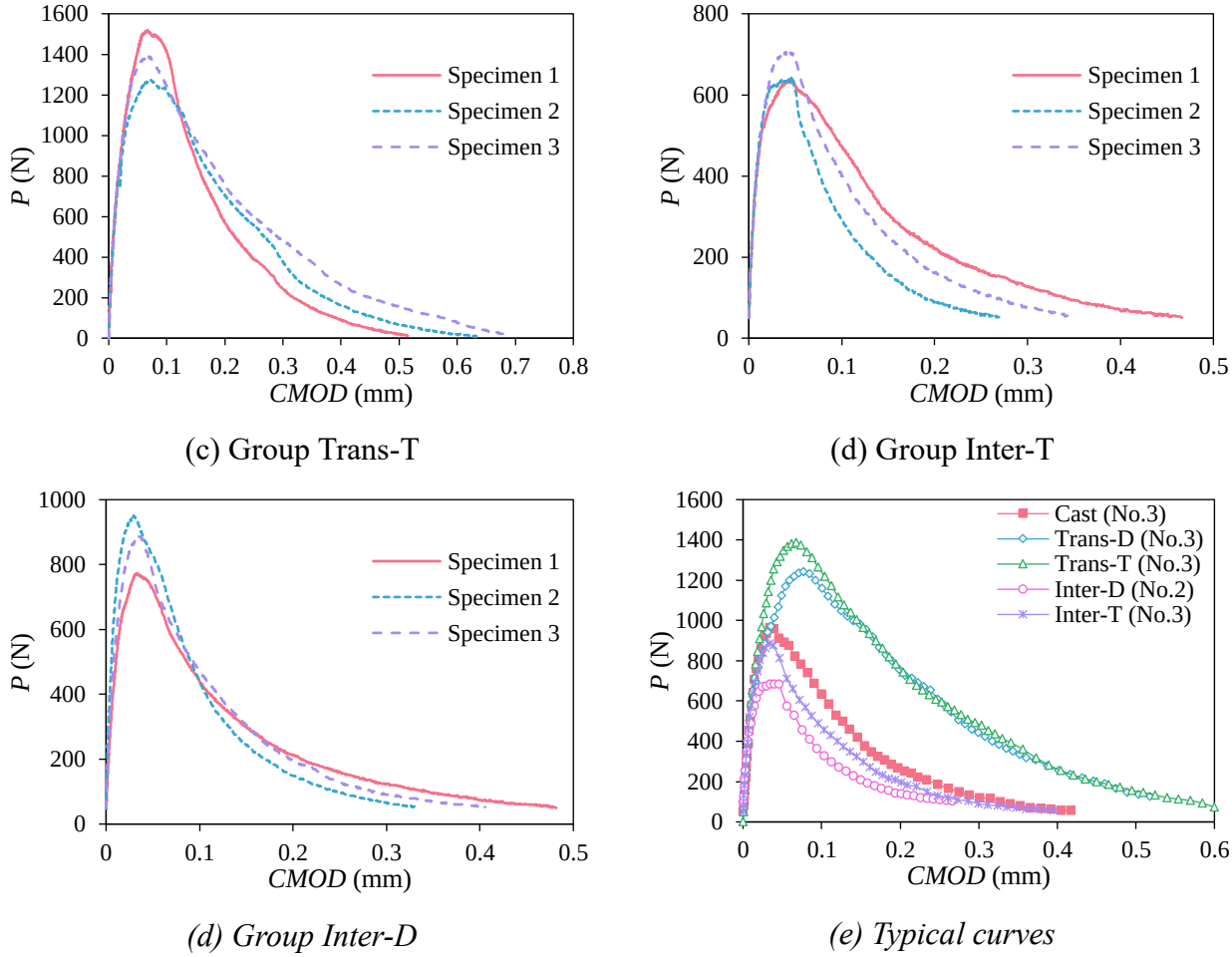

(c) Group Trans-T

(d) Group Inter-T

(d) Group Inter-D

(e) Typical curves

Fig. 5 Individual and typical load-*CMOD* curves of each group of specimens.

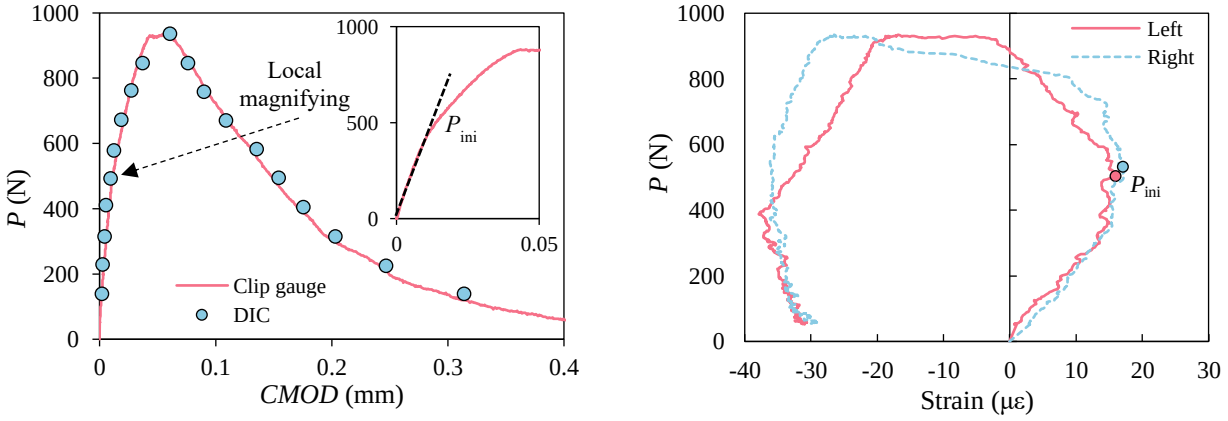

(a) Clip gauge and DIC

(b) Strain gauge

Fig. 6 Comparison of results determined using different measuring methods.

Fig. 7 presents the initial cracking load (P_{ini}) and peak load (P_c) of the cast and 3D-printed specimens. Since the determination of transition point from the initial linear section to the nonlinear section of load-*CMOD* curve is accompanied by subjectivity in practice [50], the results of P_{ini} obtained from two strain gauges shown in (see Fig. 6 (b)), *i.e.*, the smaller value between two loads corresponding to a sudden decrease of strain at the notch tip [47], were adopted in this study given that it has been widely employed for 3D printed fiber-reinforced concrete [30]. Taking the results of

Group Cast as a reference, P_{ini} of Groups Trans-D and Trans-T has no clear change, while those of Groups Inter-D and Inter-T drop obviously (about -34.8% and -16.8% respectively). Regarding P_c, there is a rise for Groups Trans-D and Trans-T (about 21.4% and 36.3% respectively) and a decline for Groups Inter-D and Inter-T (about -35.2% and -14.9% respectively). The ratios of P_{ini} to P_c for Groups Cast, Inter-D and Inter-T are near 0.55-0.57, while those of Group Trans-D and Trans-T are near 0.46-0.48. The smaller P_{ini}/P_c ratio indicates that the stable crack growth stage accounts for a larger proportion of the whole crack growth process.

The additive manufacturing process makes the pore shape of the material elongated after extrusion and the pore connectivity enhanced due to the vibration-free process [23], which causes the reduction of interlayer bond strength of 3DPC [51]. Therefore, it has little difficulty to know why the printed specimens with inter-layer fracture have a lower P_{ini} and P_c compared with the mold-cast specimen. Interestingly, P_c reflecting the bearing capacity of the beam is increased for the printed specimens with trans-layer fracture, which seems to be inconsistent with the poor pore structure induced by the extrusion-based fabricating method [15, 16]. This agrees well with the findings by other researchers [21, 32-34] that the flexural bearing capacity of 3DPC loaded in the direction perpendicular to layers is higher than that of cast concrete.

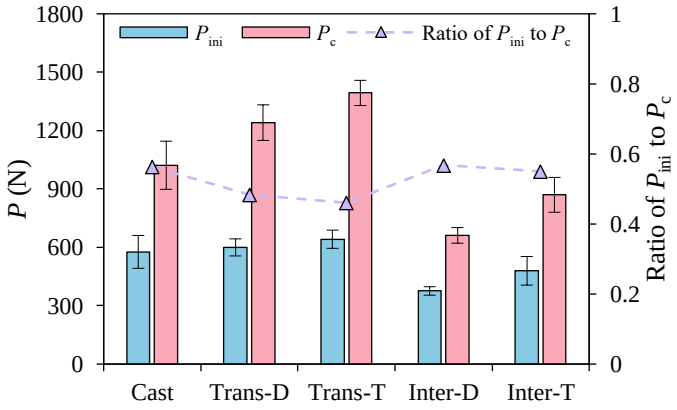

Fig. 7 Initial cracking and peak load of cast and 3D-printed concrete specimens.

3.2. Crack propagation

DIC is an optical image measuring technique to obtain non-contact full-field deformation and has been widely employed to detect the crack propagation of concrete [37]. Taking a typical specimen at the peak load as an example, the 3D plot of X-displacement (u) field measured by DIC is presented in Fig. 8a. Unlike the printing direction, X and Y coordinates (see Fig. 4a) represented the direction parallel to the initial notch (crack growing) and perpendicular to the initial notch (crack opening) on the observation surface, respectively. The crack opening displacement (COD) can be estimated by the extent of horizontal displacement jump and the crack tip can be considered as the location where the jump disappears [36, 38, 39]. As seen in Fig. 8a, the crack mouth (y = 0 mm) and tip (y = 20 mm) opening displacement (*CMOD* and *CTOD*) and the crack extension Δa can be measured directly using

the DIC analysis without instrumenting the crack for additional precise measurements. By comparing the *CMOD* results measured by DIC and clip gauge (see Fig. 6a), the good consistency can be found, proving the accuracy of DIC results. Fig. 8b plots the locally amplified and planarized displacement distribution near the notch tip (y = 20 mm). A distinct displacement jump appears around the center notch, which is caused by the crack opening. Away from the center position, the displacement distribution becomes almost smooth, suggesting that this part of the material is still in an elastic state and no cracks propagate [37, 52]. COD can be determined by subtracting u at both sides of the crack face, which is equal to about 0.025 mm. The crack tip can be defined as the location where the whole displacement becomes continuous, which is equal to about 41.4 mm.

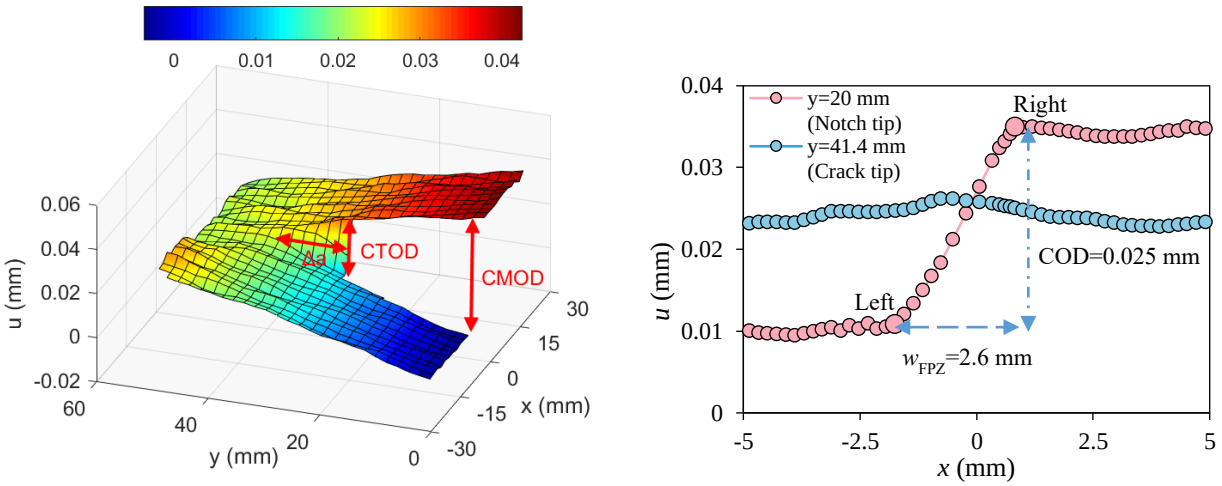

(a) 3D view (b) Plane view

Fig. 8 Determination of crack propagation from the x-displacement u.

It is difficult and time-consuming to find the exact location with continuous displacement directly from the measured displacement field, so it needs to extract the COD profile first, and then determine the position of the crack tip according to the point where COD is zero. The COD profiles of all specimens were extracted and processed from the measured displacement field [53, 54] and one typical result of each group is analyzed and plotted in Fig. 9. Compared to cast concrete, cracks of the printed concrete are easier to propagate in the opening direction rather than in the growing direction. Fig. 10a shows the mean values of critical *CMOD* and *CTOD* (denoted as $CMOD_c$ and $CTOD_c$) for all groups measured with clip gauge and DIC, respectively, and their ratios $CTOD_c/CMOD_c$. The changing trend of these values in different groups of specimens is basically similar: those in Groups Trans-D and Trans-T are higher than those in Groups Cast, Inter-D and Inter-T. The critical crack opening displacement denotes the limit, beyond which unstable crack propagation starts [39]. The larger values for the printed specimens with trans-layer fracture imply that the threshold from stable crack propagation to unstable fracture is greater, consistent with the phenomenon that the stable crack propagation stage accounts for a larger proportion during the whole

loading process.

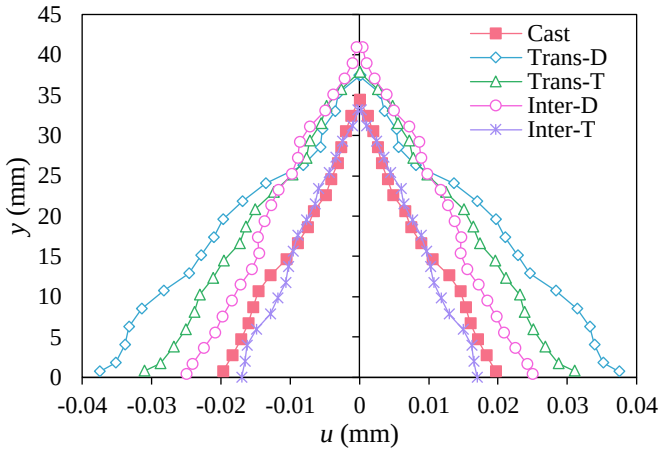

Fig. 9 COD profiles of all groups at the peak load.

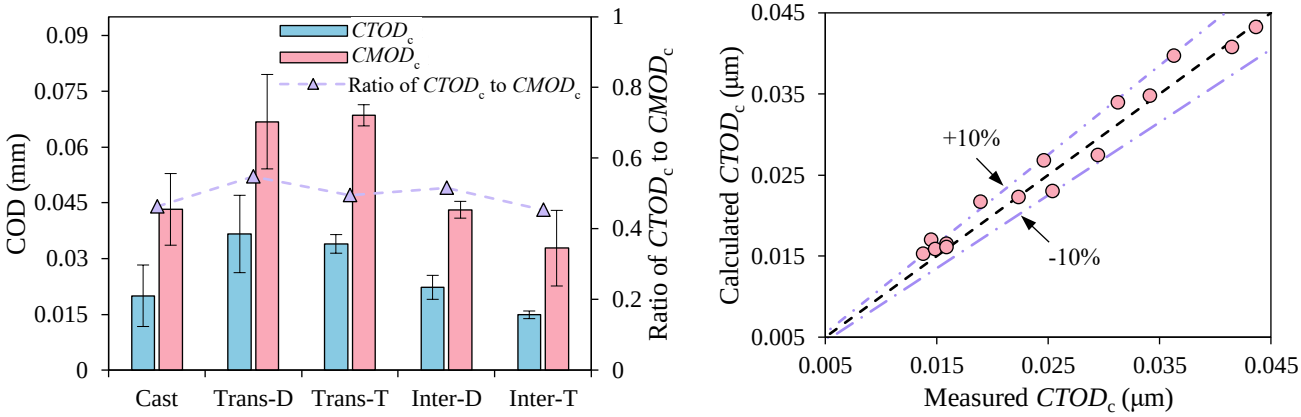

(a) Measured $CMOD_c$ and $CTOD_c$ (b) Calculated $CTOD_c$

Fig. 10 Critical crack opening displacement at the peak load.

The critical crack length (a_c) is equal to the sum of a_0 and Δa. As seen in Fig. 11a, the measured a_c of the mold-cast and printed specimens remains at a stable level (about 35.6 mm) considering the test error, except for the results of Group Inter-D (about 38.5 mm). This reveals that the poor bond strength of layer-interface results in an increased crack growth length along the interface rather than perpendicular to the interface. The critical crack extension of 3DPC declined with the rising layer heights (8-12 mm) [22].

The fracture response of specimens can be predicted by some existing fracture mechanics models for concrete, such as two parameter fracture model (TPFM) [55] and double-*K* fracture model (DKFM) [47, 50]. In the TPFM model, a_c of concrete (denoted as a_c^{TP}) can be determined from the Young's modulus (E_c^{TP}) and unloading compliance (C_u, equal to $CMOD_c/P_c$ in this study) using an iteration process as follows [55]:

$$E_c^{TP} = \frac{6Sa_c^{TP}V_1(\alpha_c^{TP})}{C_u D^2 t} \quad (1)$$

where S, D and t denote the span, depth, and thickness of the beam, respectively.

$$V_1(\alpha_c^{TP}) = 0.76 - 2.28\alpha_c^{TP} + 3.87(\alpha_c^{TP})^2 - 2.04(\alpha_c^{TP})^3 + 0.66/(1-\alpha_c^{TP})^2 \quad (2)$$

where $\alpha_c^{TP} = (a_c^{TP}+h_0)/(D+h_0)$, h_0 is the thickness of the holder of clip gauge.

E_c^{TP} can be estimated from Eqs. (1) and (2) by replacing α_c^{TP} and C_u with α_0 ($(a_0+h_0)/(D+h_0)$) and the initial compliance C_i, respectively [55]. In the DKFM, based on linear asymptotic superposition assumption, a_c^{DK} and E_c^{DK} can be calculated by inputting the measured P_c and $CMOD_c$ into the equations below [47, 50].

$$a_c^{DK} = \frac{2(D+h_0)}{\pi}\arctan\sqrt{\frac{tE_c^{DK}}{32.6(P_c+0.5mg)}CMOD_c - 0.1135} \quad (3)$$

$$E_c^{DK} = \frac{1}{tC_i}[3.70 + 32.60\tan^2(\frac{\pi}{2}\frac{a_0+h_0}{D+h_0})] \quad (4)$$

where m is the mass of beam between the supports, and g is the acceleration due to gravity (9.81 m/s^2).

In the TPFM model, $CTOD_c$ of concrete can also be calculated based on linear elastic fracture mechanics theory as follows [55]:

$$CTOD_c^{TP} = CMOD_c \times \left\{\left(1-\frac{a_0}{a_c^{TP}}\right)^2 + \left(1.081-1.149\frac{a_c^{TP}}{D}\right)\left[\frac{a_0}{a_c^{TP}} - \left(\frac{a_0}{a_c^{TP}}\right)^2\right]\right\}^{1/2} \quad (5)$$

Given that the measurement of 3DPC performance is mainly based on the specifications and models of ordinary concrete, its rationality needs to be further verified by tests [9]. A comparison of the calculated and measured values for $CTOD_c$ and a_c are displayed in Fig. 10b and Fig. 11b, respectively, indicating a good agreement with relative errors of smaller than ±10%, which suggests that the TPFM and DKFM models are still applicable to predict $CTOD_c$ and a_c for 3DPC. As seen in Fig. 11b, a_c calculated from DKFM is closer to the measured a_c than a_c calculated from TPFM. The measured values of a_c from DIC are mostly lower than the calculated ones. A similar finding was reported in Ref. [56], which was ascribed to the existence of nonlinear FPZ ahead of the crack tip in concrete, affecting the fracture parameters based on linear assumption.

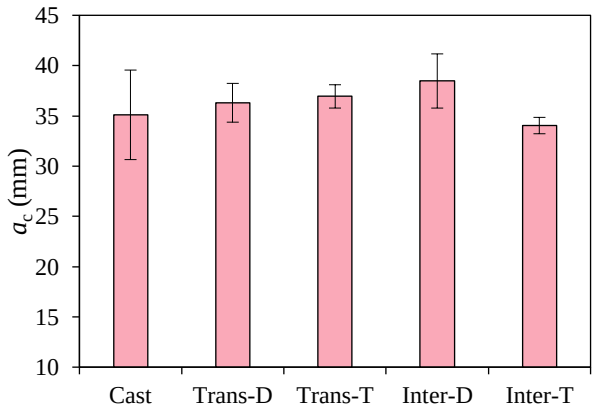

(a) DIC measured results

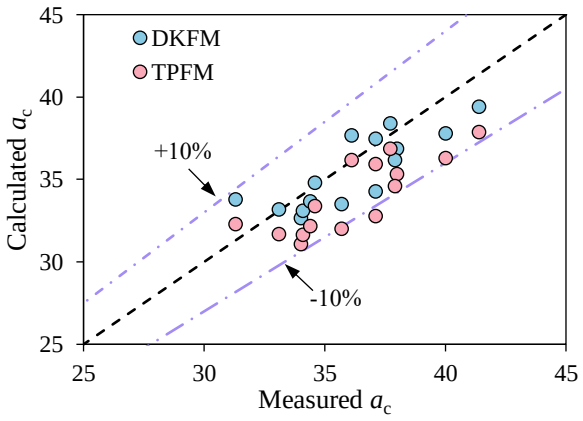

(b) Calculated results

Fig. 11 Critical crack length at peak load determined by different methods.

3.3. Fracture process zone

The microcracked area ahead of the traction-free crack tip in concrete is generally defined as FPZ, which results in a certain nonlinearity in fracture behavior of concrete, and thus has received widespread attentions [57]. The geometric characteristics of FPZ can be characterized qualitatively by using the strain field [36, 38, 54, 58, 59]. The Lagrangian strain fields in x-direction (ε_{xx}) can be calculated using the DIC measured displacement fields as follows [36]:

$$\varepsilon_{xx} = \frac{du}{dx} + \frac{1}{2}\left[\left(\frac{du}{dx}\right)^2 + \left(\frac{dv}{dy}\right)^2 \right] \tag{6}$$

where u and v are the displacements in the x and y directions, as demonstrated in Fig. 4a.

The typical strain fields above the notch of different group specimens are presented in Fig. 12, where FPZ can be considered as the area of strain localization [36, 54, 57, 60]. The strain concentration is significant near the notch tip and becomes weak away from the notch tip. These figures visually show that in comparison with Group Cast, the diffusion ranges of the localized zone in Groups Trans-D and Trans-T are wider whereas those in Groups Inter-D and Inter-T are narrower.

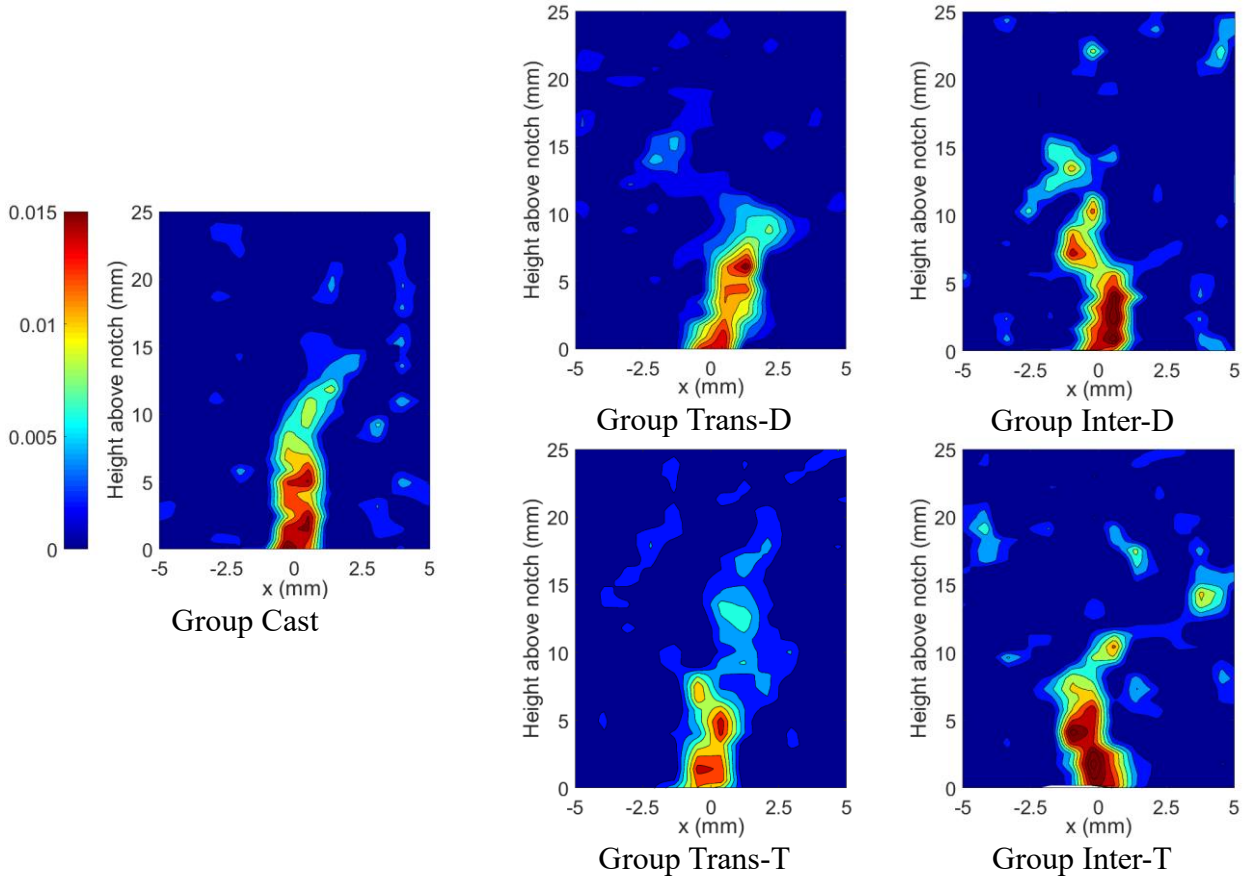

Fig. 12 Strain localization zones of different group specimens at peak load.

To further quantitatively describe the FPZ size, the measured displacement field seems to be better than the strain field [37, 54, 57]. When calculating the strain based on the reference length, the discontinuity can lead to strain deviation, especially near FPZ [37]. The FPZ tip can be regarded as

the location where the crack opening becomes zero. Since FPZ is usually fully developed at post-peak loading level [54, 61], the rear of FPZ (*i.e.*, the tip of traction-free crack) remains at the notch tip and does not move forward at the peak load. The FPZ length at the peak load is equal to the crack growth length (Δa).

Besides the cohesive stresses distributing over the FPZ length, the crack-tip blunting induced by the FPZ width w_{FPZ} can also cause quasi-brittle and elastic–plastic fracture behavior of concrete [62]. As seen in Fig. 8b, the start and end of the displacement jump can be regarded as the left and right boundary position of FPZ, and w_{FPZ} can be defined as the distance between them, which is about 2.6 mm. Generally, the setting of parameters related to the subset affects the boundary range of DIC measurement [48]. The reduction of w_{FPZ} with distance from the notch becomes prominent beyond a certain crack extension [36]. Considering these, w_{FPZ} at a location 5 mm above the notch was adopted to facilitate a comparison of the different group specimens in this study. Moreover, the area of FPZ was calculated by the product of its length and width [36, 38, 63].

Fig. 13 depicts the FPZ width and area of the mold-cast and printed specimens. The FPZ width of Groups Trans-D and Trans-T is about 1.32 and 1.40 times that of Group Cast, while that of Groups Inter-D and Inter-T is about 0.8 times. The FPZ area has the same variation tendency between each group as the FPZ width. Since the FPZ length does not change significantly with the construction mode or the layer orientation (see Fig. 11a), it can be inferred that the change of the FPZ area is more dependent on its width than its length. It should be noted that the FPZ size of quasi-brittle materials is generally dependent on the specimen size and the initial notch-to-depth ratio [54, 62]. Besides, the FPZ size measured by DIC is highly affected by the image resolution: a higher image resolution leads to a smaller FPZ size [64]. Thus, the FPZ size reported with the same specimen geometry is used only to compare the fracture behavior of different construction methods and layer directions in this study.

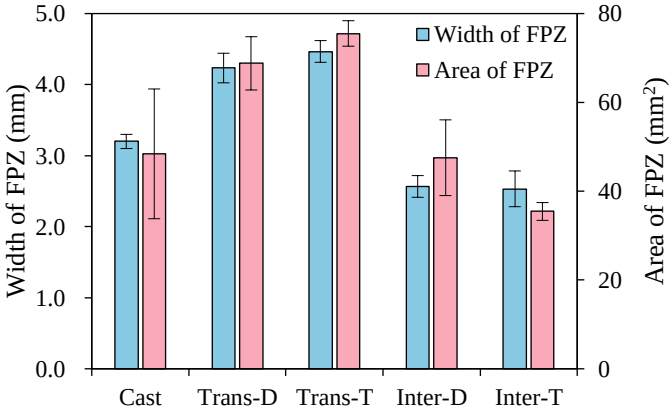

Fig. 13 Width and area of fracture process zone (FPZ) of cast and 3D-printed concrete specimens.

3.4. Fracture energy

The toughening mechanism in FPZ is well known, in relation to the variation of energy dissipation. As an important parameter to quantify the fracture property of materials, the fracture energy (G_f)

denotes the energy required for the crack extension per unit area [49, 65]. According to work-of-fracture method, G_f can be estimated from the area under the complete load-displacement curve (W_0) as follows [66]:

$$G_f = \frac{(W_0 + mg\delta_0)}{(D - a_0)t} \tag{7}$$

where δ_0 is the deflection at the final failure, and m is the mass of the beam between supports which can be estimated by the density as listed in Table 2.

Fig. 14 presents the fracture energy (G_f) of all group specimens. The fracture energy of the mold-cast specimen is about 92.8 N/m, which is slightly higher than that of normal concrete (about 76.81-85.3 N/m) determined by Su *et al*. [67]. This is because the w/c ratio of 3DPC is relatively small, which leads to more energy consumption [49]. G_f of the printed specimens in Groups Trans-D and Trans-T are about 159.5 N/m and 178.7 N/m, respectively, which are 71.8% and 92.6% respectively higher than that of the cast specimen. The interfaces caused by the printing process act as crack barriers when they are perpendicular to crack propagation, resulting in extra energy dissipation to across them. Nair *et al*. [22] reported that the strain energy release rate was higher for specimens printed using smaller layer heights because of more interfaces. The increased fracture energy in 3D printed fiber-reinforced concrete was also reported in Ref. [30], where the increment of the printed specimens loaded in Y- and Z-directions was 23.4% and 36.2%, respectively. The smaller difference can be explained by the fact that the main energy dissipation mechanism of 3D printed fiber reinforced concrete is the bridging effect of fibers. G_f of Groups Inter-D and Inter-T are approximately 55.6 and 66.4 N/m, which are 40.1% and 28.5% lower than that of Group Cast. The porous interlayer without vibration and compaction makes it easier for the crack to expand directly along the interface, reducing the energy consumed by crack deflection or branch.

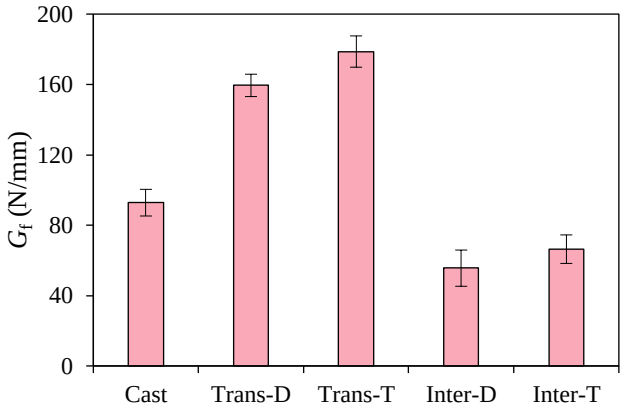

Fig. 14 Fracture energy of cast and 3D-printed concrete specimens.

3.5. Double-K fracture toughness

The mode-I fracture toughness K_I of concrete is another important fracture parameter, denoting the

fracture resistance of concrete under external load. To further analyze different stages of fracture behavior of 3DPC, the double-*K* fracture criterion [50] was adopted here. In the DKFM model, the entire fracture process of quasi-brittle materials is divided into three stages using two fracture toughness parameters (i.e., initial cracking toughness K_{Ic}^{ini} and unstable fracture toughness K_{Ic}^{un}): crack initiation ($K_I = K_{Ic}^{ini}$), stable crack propagation ($K_{Ic}^{ini} < K_I < K_{Ic}^{un}$) and unstable fracture failure ($K_{Ic}^{un} < K_I$). K_{Ic}^{ini} of concrete can be calculated from the initial cracking load P_{ini} and the initial crack length a_0 as follows [47]:

$$K_{Ic}^{ini} = 1.5\frac{(P_{ini} + 0.5mg)S}{D^2 t}\sqrt{a_0}F(\alpha_0) \tag{8}$$

where $F(\alpha_0)$ is the geometric shape function that can be determined using the following equation for a notched beam with a *S*/*D* ratio of 4.

$$F(\alpha_0) = \frac{1.99 - \alpha_0(1-\alpha_0)(2.15 - 3.93\alpha_0 + 2.7\alpha_0^{\,2})}{(1+2\alpha_0)(1-\alpha_0)^{3/2}} \tag{9}$$

Besides, the value of K_{Ic}^{un} can also be obtained by replacing P_{ini} and a_0 with P_c and a_c in Eqs. (8) and (9). The formula for calculating the fracture toughness is derived based on fracture mechanics theory, which is mainly related to the geometric type of the specimen and has been successfully used in the studies for other quasi-brittle materials [58, 68]. Thus, it can be reasonably considered that its applicability is not affected by the special proportion of 3DPC.

Fig. 15 depicts the calculated K_{Ic}^{ini} and K_{Ic}^{un} of the cast and printed specimens. Regarding K_{Ic}^{ini}, the results of the trans-layer specimens (Groups Trans-D and Trans-T) are similar to those of the cast specimen and remain at a stable range of 0.304-0.329 MPa.m$^{1/2}$, while those of the inter-layer specimens (Groups Inter-D and Inter-T) are 22.3% lower (about 0.244-0.249 MPa.m$^{1/2}$). K_{Ic}^{ini} of materials reflects the ability to resist cracking. Since the interface strength of 3DPC is commonly less than the bulk material strength, it is more likely to crack when the main crack propagation direction is along the interlayer. While in the case of the main crack propagation direction being perpendicular to the interlayer, the bulk strength of the material still dominates the initial cracking behavior. As can be seen, the variation law of K_{Ic}^{un} among the cast specimens and printed specimens is consistent with that of G_f, *i.e.*, the values of the printed specimens with trans-layer/inter-layer fracture are higher or lower than those of the cast specimens, respectively. The range of this rise and drop is about 30.3-41.1% and 20.7-25.5%. The ratios of K_{Ic}^{ini} to K_{Ic}^{un} for all groups are helpful to characterize the stable crack growth stage and plotted in Fig. 15. In comparison with Group Cast, the ratios of the printed specimen with inter-layer fracture remain unchanged (about 0.29) whereas those of the printed specimen with inter-layer fracture become lower (about 0.21). This indicates that the relatively inferior interface expands the extent of stable crack propagation stage (also considered as delaying the rapidly failure stage) for 3DPC when it bears a load perpendicular to layers.

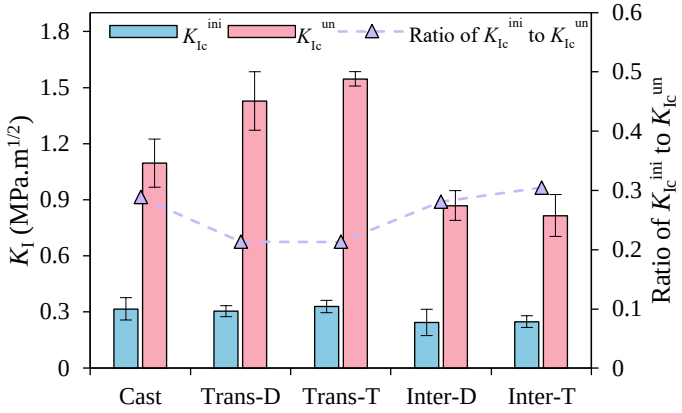

Fig. 15 Initial cracking and unstable fracture toughness of cast and 3D-printed concrete specimens.

The fracture parameters determined in this study indicate that the resistance and energy consumption of a crack passing through printed layers is greater than when it passes through the bulk material and along the printed layers. It is worth noting that the print interlayer characteristics depend on various factors such as the ink material (*e.g.* type and distribution of fibers, aggregate particle size and volume fraction), printing parameters (*e.g.* time interval, layer height, print path), and printing and curing environments (*e.g.* temperature and humidity). For instance, in this study, the resistance of cracking through deposition layers (Group Trans-D) was slightly lower than that through translation layers (Group Trans-T). Considering the effect of the gravity factor of the printed filaments, the bond strength between the printed layers along Z direction should theoretically be greater than that along Y direction. This can be explained by the fact that under the design of the print nozzle height, there is also a certain amount of contact stress between the parallel filaments along Y-direction, and the Group Trans-D specimens were printed for a relatively long period of time, which may also adversely affect the interlayer bonding performance. Additionally, the variability of the properties of printed specimens is generally further aggravated as the printed specimen has many extra interlayer interfaces than the cast one. Hence, to comprehensively understand the evolution law of 3DPC fracture parameters, more experiments are required to study the fracture properties of 3DPC with various mix proportions, printing parameters, printing and curing environments. The special focus of this study is placed on the influencing mechanism of two cracking patterns (*i.e.*, trans-layer and inter-layer) on the fracture behavior of the printed hardened concrete, which is discussed in depth below.

4. Discussion

Through the analysis of above experimental results, fracture mechanisms of cast and 3D printed concrete are schematically illustrated in Fig. 16. As seen in Fig. 16a, the FPZ of concrete materials is a damage zone where there are many fracture toughening mechanisms, such as microcracking, crack deflection, aggregate bridging and crack blunting, which result in the energy being dissipated [36, 61, 65]. The layer-by-layer stacking process of 3D concrete printing leads to the relatively poor interlayer adhesion due to the lack of interlayer moisture, air entrapment, adverse thixotropy and lack of surface

roughness [51]. Among them, the surface moisture of filaments plays an important role as it would cause some air voids left near the interlayer [13, 51]. By analyzing the pore structure of 3DPC, it can be found that the porosity near the interlayer is obviously higher than other parts [35]. Besides, the pore shape of the printed specimens tends to be elongated after extrusion, deposition, and translation of the filaments [35, 69]. These flat ellipsoidal pores can be regarded as initial defects induced during the printing process and pore-induced cracking behavior would affect the mechanical properties of material [16]. As a result, the resistance and energy required for crack propagation in these weak interfaces are lower (about 20.7-25.5% and 28.5-40.1%, respectively) than that in the bulk material. Therefore, 3DPC has an additional fracture mechanism (interlaminar cracking) than cast concrete.

When the loading direction is perpendicular to the printed layer, *i.e.*, trans-layer fracture (see Fig. 16b), the interlaminar cracking direction is orthogonal to the ligament direction, which helps to relieve the stress concentration and plays a negative role in main crack extension, resulting in a wider FPZ. In this study, both a significant increase of crack opening parallel to the interface, and a larger proportion of stable crack propagation (*i.e.*, delaying the onset of unstable failure) can provide supporting evidence. As such, the interlaminar cracking can be regarded as a toughening mechanism that enhances strength, energy consumption and deformability. Whereas, when the loading direction is parallel to the printed layer, *i.e.*, inter-layer fracture (see Fig. 16c), the interlaminar cracking direction is consistent with the ligament direction, which facilitates the main crack propagation and reduces the emergence of other microcracks, leading to a narrower FPZ. Accordingly, its fracture behavior becomes relatively more brittle, and the fracture properties are weakened.

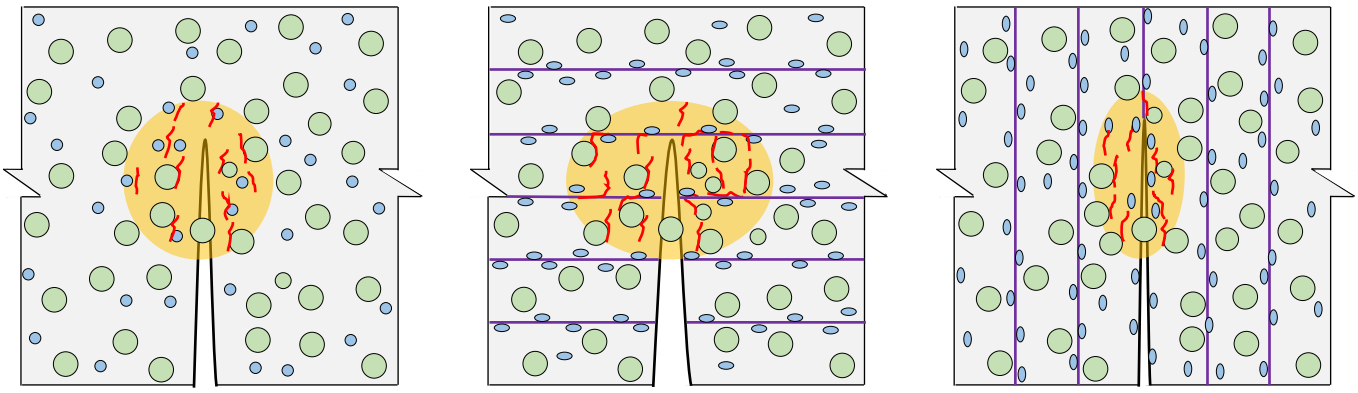

(a) Cast (b) Trans-layer fracture (c) Inter-layer fracture

Fig. 16 Schematic diagrams of fracture mechanism of the cast and 3D printed concrete (*Notes:* red curve, purple line, green circle, blue circle, and orange circle denote the micro-crack, interface, aggregate, air void, and FPZ, respectively. All of these are generalized for illustrative purposes only and do not represent the real size).

Since the existence of FPZ is the primary reason of the quasi-brittle fracture behavior of concrete, its characteristics have a strong relation with the fracture response of concrete [36, 54, 61, 63]. There

are mainly two methods for the analysis of nonlinear fracture behavior of quasi-brittle materials, i.e., the energy balance method, and the stress intensity method [52, 70]. Correspondingly, the fracture energy and critical stress intensity factor (*i.e.*, unstable fracture toughness) are regarded as two most basic and important fracture parameters. The relationships between the FPZ area and different fracture parameters (G_f and K_{Ic}^{un}) of the cast and printed specimens are depicted in Fig. 17. There are positive correlations between G_f and K_{Ic}^{un} and the FPZ area at the peak load. For quasi-brittle materials, the FPZ area represents the extent of the nonlinear zone in the region ahead of a real cohesion-free crack. Thus, the larger area of FPZ indicates that the concrete material can experience relatively more inelastic deformation in the crack-opening direction before a macro-crack is formed. The satisfactory linear correlations suggest that the anisotropy of fracture parameters of 3DPC is dependent on the FPZ properties, specifically the interlaminar cracking mechanism. Since the fracture energy is related to the loading process, correlating it with the FPZ area under a certain loading moment is only to further clarify the fracture mechanism of 3DPC by combining the global and local responses.

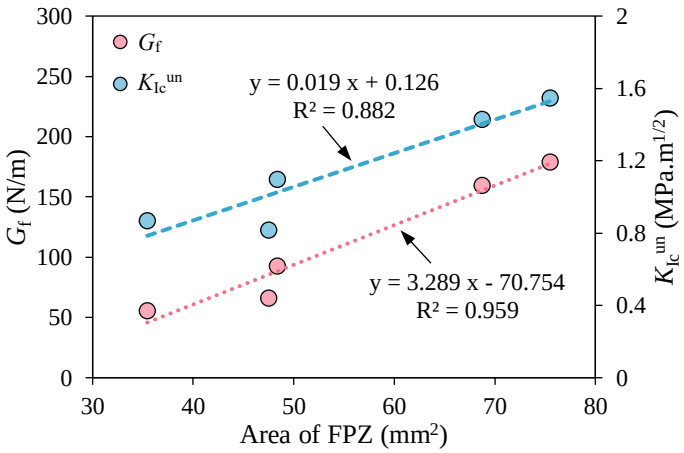

Fig. 17 Correlations between the FPZ area and different fracture parameters.

Generally, more mixture proportions can yield more convincing conclusions for heterogeneous materials, like concrete. While a lot of existing studies on 3DPC [15, 35, 71] only use one mix ratio since they focus on the influence of printing process (*i.e.*, layered structures after hardening) on the concrete properties. Given that the current study aims to explore the influence of layer-by-layer printing process on concrete fracture mechanism, two fracture patterns (trans-layer fracture and inter-layer fracture) induced by layered structures were taken as the main parameter variables and thus only one mix proportion was adopted. Compared with 3D printed fiber reinforced concrete [22, 30], similar fracture response was found for the 3DPC specimens loaded in different directions, suggesting the applicability of findings of this study. Certainly, it is necessary to study the effects of printing and material parameters, curing methods and specimens' geometric factors (including size effect and boundary effect) on the two process-induced fracture patterns for 3DPC in future study.

Additive manufacturing process causes more interlayer cracking in the fracture process of concrete

under external loading. It can make the fracture behavior of concrete more brittle, but it can also increase the ductility of concrete, depending on the loading direction and the interface between adjacent layers. Compared with traditional cast-in-mold technology, one of the biggest advantages of 3D printing technology is that it can be customized to generate various special-shaped spatial structures, which bring about many new design capabilities and possibilities [2]. In the setting of printing parameters or printing path, it is suggested to take advantage of the characteristics of interlayer cracking to release the stress concentration and improve the deformation capacity, making the process-induced interfaces become a toughening approach rather than an inherent defect.

In terms of printing parameters, taking the filament height as an example, a lower nozzle height squeezes the printing filament, causing the filament to decrease in height and increase in width. The interface between layers becomes denser under pressure, which increases the adhesion and crack resistance of a single interlayer and results in a greater number of interlayer cracks due to more layers. Therefore, the flexural and fracture properties of 3D printed concrete specimens with a lower layer height would be better [22]. If there are remarkable differences in the number and mechanical properties of process-induced interfaces in the specimens, the anisotropy of mechanical behavior of 3DPC will be changed [25]. Besides, it is necessary to balance other aspects related to nozzle height, such as the fresh-state buildability, the applied nozzle pressure and printing time. Regarding the printing path, various topological patterns and bio-inspired design for 3D concrete printing can offer convenience [72]. For instance, inspired by the dactyl club of mantis shrimp, Liu *et al.* [73] designed four printing patterns with different pitch angles causing different extent of local stress distribution as the crack propagates during the impact loading process. Inspired by the natural nacre, Ye *et al.* [74] developed a 3D printed concrete member improved by extrinsic toughening and hierarchical assembly, mainly due to the limited interlamellar sliding and strain relaxation. In future printing process design of 3DPC, it would be beneficial to refer to other naturally orthotropic materials, e.g., wood and bone, which are skilled in taking advantage of the increased toughness induced by defect/laminae alignment to obtain overall toughness, although the ingredients may be individually fragile. In general, 3D concrete printing technology brings new opportunities and possibilities to the construction industry. The rational use of its own characteristics to produce customized fracture and failure behavior can facilitate the development of higher performance additive manufacturing components and structures.

5. Conclusions

In this study, three-point bending notched beam tests were carried out to explore the fracture behavior of 3DPC, with special focus on the effects of printed specimens with trans-layer fracture and inter-layer fracture. The following conclusions can be drawn from the tests and analysis:

(1) The resistance and energy required for crack propagation in these interfaces are lower than that in the bulk material without process-induced interfaces. The fracture process of 3DPC is the same as

that of cast-in-mold concrete, including three stages of crack initiation, stable propagation, and unstable fracture. The crack propagation across the interlayers amplifies the stable propagation process (*i.e.*, delays the unstable failure), while the crack propagation along the interlayers facilitates the crack initiation.

(2) Compared to crack growth, the crack opening of printed specimens is more pronounced in the critical state, especially when the load is perpendicular to the interlayer direction. The good agreement between a_c and $CTOD_c$ measured by DIC, and the predictions based on the existing concrete fracture mechanics models suggests that they are still suitable for 3DPC.

(3) In comparison with that of the cast specimens, the fracture energy of the printed specimens with trans-layer fracture increases by about 71.8-92.6%, while that of the printed specimens with inter-layer fracture drops by about 28.5-40.1%. The same variation tendency is found for the unstable fracture toughness with increase and decrease ranges of about 30.3-41.1% and 20.7-25.5%, respectively. The initial cracking toughness reduces by about 22.3% only when the interlayer orientation is parallel to the loading direction.

(4) For 3DPC, the FPZ area goes up with trans-layer fracture and drops with inter-layer fracture, which is mainly controlled by the FPZ width. The layer-by-layer printing process additionally introduces interlaminar cracking as a fracture mechanism in concrete FPZ. It can play a toughening role if the main crack propagates through the interlayer rather than along the interlayer, as it helps relieve the stress concentration and improve the deformability. In the printing process design, it is recommended to take full advantage of this property to make the process-induced interface turn into a toughening means rather than an inherent defect, which can be inspired by nature.

This experimental study is mainly focused on the fracture behavior of 3DPC in relation to layer-by-layer printing process (*i.e.*, trans-layer fracture and inter-layer fracture). For future research, it is necessary to investigate the influences of other factors such as mix proportion, printing parameters, printing and curing environments, specimen size and notch depth on fracture behavior and mechanical properties, as well as numerical simulations accounting for the multi-layer characteristics, which can gain more insights into the fracture process and damage mechanism. The potential exploitation of toughening means of 3D printed member through its the process-induced multilayer interfaces also needs to be further explored or validated.

Acknowledgements

The financial support from the National Natural Science Foundation of China (No. 52078358) and National Key R&D Program of China (2022YFC3803400, 2022YFE0198300) is gratefully appreciated.

References

[1] V. Mechtcherine, V.N. Nerella, F. Will, M. Nather, J. Otto, M. Krause, Large-scale digital concrete construction-CONPrint3D concept for on-site, monolithic 3D-printing, Automat Constr, 107 (2019) 102933.

[2] T. Wangler, N. Roussel, F.P. Bos, T.A.M. Salet, R.J. Flatt, Digital Concrete: A Review, Cement and Concrete Research, 123 (2019) 105780.

[3] V. Mechtcherine, R. Buswell, H. Kloft, F.P. Bos, N. Hack, R. Wolfs, J. Sanjayan, B. Nematollahi, E. Ivaniuk, T. Neef, Integrating reinforcement in digital fabrication with concrete: A review and classification framework, Cement Concrete Comp, 119 (2021) 103964.

[4] F. Craveiro, J.P. Duarte, H. Bartolo, P.J. Bartolo, Additive manufacturing as an enabling technology for digital construction: A perspective on Construction 4.0, Automat Constr, 103 (2019) 251-267.

[5] C. Menna, J. Mata-Falcon, F.P. Bos, G. Vantyghem, L. Ferrara, D. Asprone, T. Salet, W. Kaufmann, Opportunities and challenges for structural engineering of digitally fabricated concrete, Cement and Concrete Research, 133 (2020) 106079.

[6] G. De Schutter, K. Lesage, V. Mechtcherine, V.N. Nerella, G. Habert, I. Agusti-Juan, Vision of 3D printing with concrete - Technical, economic and environmental potentials, Cement and Concrete Research, 112 (2018) 25-36.

[7] C. Zhang, V.N. Nerella, A. Krishna, S. Wang, Y.M. Zhang, V. Mechtcherine, N. Banthia, Mix design concepts for 3D printable concrete: A review, Cement Concrete Comp, 122 (2021) 104155.

[8] H. Liu, T. Ding, J. Xiao, V. Mechtcherine, Buildability prediction of 3D–printed concrete at early-ages: A numerical study with Drucker–Prager model, Additive Manufacturing, 55 (2022) 102821.

[9] V. Mechtcherine, K. van Tittelboom, A. Kazemian, E. Kreiger, B. Nematollahi, V.N. Nerella, M. Santhanam, G. de Schutter, G. Van Zijl, D. Lowke, E. Ivaniuk, M. Taubert, F. Bos, A roadmap for quality control of hardening and hardened printed concrete, Cement and Concrete Research, 157 (2022) 106800.

[10] S.D. Hou, Z.H. Duan, J.Z. Xiao, J. Ye, A review of 3D printed concrete: Performance requirements, testing measurements and mix design, Construction and Building Materials, 273 (2021) 121745.

[11] S.A.O. Nair, S. Panda, M. Santhanam, G. Sant, N. Neithalath, A critical examination of the influence of material characteristics and extruder geometry on 3D printing of cementitious binders, Cement Concrete Comp, 112 (2020) 103671.

[12] R.J.M. Wolfs, F.P. Bos, T.A.M. Salet, Hardened properties of 3D printed concrete: The influence of process parameters on interlayer adhesion, Cement and Concrete Research, 119 (2019) 132-140.

[13] J.G. Sanjayan, B. Nematollahi, M. Xia, T. Marchment, Effect of surface moisture on inter-layer strength of 3D printed concrete, Construction and Building Materials, 172 (2018) 468-475.

[14] E. Keita, H. Bessaies-Bey, W.Q. Zuo, P. Belin, N. Roussel, Weak bond strength between successive layers in extrusion-based additive manufacturing: measurement and physical origin, Cement and Concrete Research, 123 (2019) 105787.

[15] J. Kruger, A. du Plessis, G. van Zijl, An investigation into the porosity of extrusion-based 3D printed concrete, Additive Manufacturing, 37 (2021) 101740.

[16] H. Liu, C. Liu, G. Bai, Y. Wu, C. He, R. Zhang, Y. Wang, Influence of pore defects on the hardened properties of 3D printed concrete with coarse aggregate, Additive Manufacturing, 55 (2022) 102843.

[17] H. Kloft, H.W. Krauss, N. Hack, E. Herrmann, S. Neudecker, P.A. Varady, D. Lowke, Influence of process parameters on the interlayer bond strength of concrete elements additive manufactured by Shotcrete 3D Printing (SC3DP), Cement and Concrete Research, 134 (2020) 106078.

[18] L.W. He, W.T. Chow, H. Li, Effects of interlayer notch and shear stress on interlayer strength of 3D printed cement paste, Additive Manufacturing, 36 (2020) 101390.

[19] B. Zareiyan, B. Khoshnevis, Effects of interlocking on interlayer adhesion and strength of structures in 3D printing of concrete, Automat Constr, 83 (2017) 212-221.

[20] G.W. Ma, Z.J. Li, L. Wang, F. Wang, J. Sanjayan, Mechanical anisotropy of aligned fiber reinforced composite for extrusion-based 3D printing, Construction and Building Materials, 202 (2019) 770-783.

[21] T. Ding, J.Z. Xiao, S. Zou, Y. Wang, Hardened properties of layered 3D printed concrete with recycled sand, Cement Concrete Comp, 113 (2020) 103724.

[22] S.A.O. Nair, A. Tripathi, N. Neithalath, Examining layer height effects on the flexural and fracture response of plain and fiber-reinforced 3D-printed beams, Cement Concrete Comp, 124 (2021)

104254.

[23] L. Ma, Q. Zhang, Z.J. Jia, C. Liu, Z.C. Deng, Y.M. Zhang, Effect of drying environment on mechanical properties, internal RH and pore structure of 3D printed concrete, Construction and Building Materials, 315 (2022) 125731.

[24] L. Dong, Y. Yang, Z. Liu, Q. Ren, J. Li, Y. Zhang, C. Wu, Microstructure and mechanical behaviour of 3D printed ultra-high performance concrete after elevated temperatures, Additive Manufacturing, 58 (2022) 103032.

[25] J. Xiao, H. Liu, T. Ding, Finite element analysis on the anisotropic behavior of 3D printed concrete under compression and flexure, Additive Manufacturing, 39 (2021) 101712.

[26] S.P. Shah, S.E. Swartz, C. Ouyang, Fracture Mechanics of Concrete: Applications of Fracture Mechanics to Concrete, Rock and Other Quasi-Brittle Materials, John Wiley & Sons, Inc., New York, 1995.

[27] J.D.M. Malan, A.S. van Rooyen, G.P.A.G. van Zijl, Chloride Induced Corrosion and Carbonation in 3D Printed Concrete, Infrastructures, 7 (2022) 1.

[28] M. van den Heever, F. Bester, J. Kruger, G. van Zijl, Mechanical characterisation for numerical simulation of extrusion-based 3D concrete printing, Journal of Building Engineering, 44 (2021) 102944.

[29] M. van den Heever, F. Bester, J. Kruger, G. van Zijl, Numerical modelling strategies for reinforced 3D concrete printed elements, Additive Manufacturing, 50 (2022) 102569.

[30] S. Yang, T. Lan, Z. Sun, M. Xu, M. Wang, Y. Feng, A predictive model to determine tensile strength and fracture toughness of 3D printed fiber reinforced concrete loaded in different directions, Theor Appl Fract Mec, 119 (2022) 103309.

[31] J. Xiao, Z. Lv, Z. Duan, S. Hou, Study on preparation and mechanical properties of 3D printed concrete with different aggregate combinations, Journal of Building Engineering, 51 (2022) 104282.

[32] T.T. Le, S.A. Austin, S. Lim, R.A. Buswell, R. Law, A.G.F. Gibb, T. Thorpe, Hardened properties of high-performance printing concrete, Cement and Concrete Research, 42 (2012) 558-566.

[33] B. Panda, S.C. Paul, L.J. Hui, Y.W.D. Tay, M.J. Tan, Additive manufacturing of geopolymer for sustainable built environment, Journal of Cleaner Production, 167 (2017) 281-288.

[34] J.H. Ye, C. Cui, J.T. Yu, K.Q. Yu, F.Y. Dong, Effect of polyethylene fiber content on workability

and mechanical-anisotropic properties of 3D printed ultra-high ductile concrete, Construction and Building Materials, 281 (2021) 122586.

[35] M. van den Heever, A. du Plessis, J. Kruger, G. van Zijl, Evaluating the effects of porosity on the mechanical properties of extrusion-based 3D printed concrete, Cement and Concrete Research, 153 (2022) 106695.

[36] S. Das, M. Aguayo, G. Sant, B. Mobasher, N. Neithalath, Fracture process zone and tensile behavior of blended binders containing limestone powder, Cement and Concrete Research, 73 (2015) 51-62.

[37] Z.M. Wu, H. Rong, J.J. Zheng, F. Xu, W. Dong, An experimental investigation on the FPZ properties in concrete using digital image correlation technique, Engineering Fracture Mechanics, 78 (2011) 2978–2990.

[38] S. Das, A. Kizilkanat, N. Neithalath, Crack propagation and strain localization in metallic particulate-reinforced cementitious mortars, Mater Design, 79 (2015) 15-25.

[39] S. Das, M. Aguayo, V. Dey, R. Kachala, B. Mobasher, G. Sant, N. Neithalath, The fracture response of blended formulations containing limestone powder: Evaluations using two-parameter fracture model and digital image correlation, Cement Concrete Comp, 53 (2014) 316-326.

[40] H.H. Zhang, J.Z. Xiao, Plastic shrinkage and cracking of 3D printed mortar with recycled sand, Construction and Building Materials, 302 (2021) 124405.

[41] GB/T 2419-2005, Standard for Test method for fluidity of cement mortar, in: GB/T 2419-2005 (Ed.), National Standard of the People's Republic of China, 2005.

[42] D.H. Murcia, M. Genedy, M.M.R. Taha, Examining the significance of infill printing pattern on the anisotropy of 3D printed concrete, Construction and Building Materials, 262 (2020) 120559.

[43] Y. Chen, Z. Chang, S. He, O. Çopuroğlu, B. Šavija, E. Schlangen, Effect of curing methods during a long time gap between two printing sessions on the interlayer bonding of 3D printed cementitious materials, Construction and Building Materials, 332 (2022) 127394.

[44] GB/T 50081-2019, Standard for test methods of concrete physical and mechanical properties, in, National Standard of the People's Republic of China.

[45] ASTM C511-21, Standard Specification for Mixing Rooms, Moist Cabinets, Moist Rooms, and Water Storage Tanks Used in the Testing of Hydraulic Cements and Concretes, in, American Society

for Testing and Materials.

[46] RILEM, TC 89-FMT Fracture Mechanics of Concrete, Determination of Fracture Parameters (KIcs and CTODc) of Plain Concrete Using Three-point Bend Tests, Materials and Structures, 23 (1990) 457-460.

[47] S.L. Xu, Q.H. Li, Y. Wu, L.X. Dong, Y. Lyu, H.W. Reinhardt, C.K.Y. Leung, G. Ruiz, S. Kumar, S.W. Hu, RILEM Standard: testing methods for determination of the double-K criterion for crack propagation in concrete using wedge-splitting tests and three-point bending beam tests, recommendation of RILEM TC265-TDK, Materials and Structures, 54 (2021) 220.

[48] Q.F. Liu, D.T.W. Looi, H.H. Chen, C. Tang, R.K.L. Su, Framework to optimise two-dimensional DIC measurements at different orders of accuracy for concrete structures, Structures, 28 (2020) 93-105.

[49] S. Khalilpour, E. BaniAsad, M. Dehestani, A review on concrete fracture energy and effective parameters, Cement and Concrete Research, 120 (2019) 294-321.

[50] S.L. Xu, H.W. Reinhardt, Determination of double-K criterion for crack propagation in quasi-brittle fracture, Part II: Analytical evaluating and practical measuring methods for three-point bending notched beams, Int J Fracture, 98 (1999) 151-177.

[51] G.M. Moelich, J. Kruger, R. Combrinck, Modelling the interlayer bond strength of 3D printed concrete with surface moisture, Cement and Concrete Research, 150 (2021) 106559.

[52] Y.X. Tang, R.K.L. Su, H.N. Chen, Energy dissipation during fracturing process of nuclear graphite based on cohesive crack model, Engineering Fracture Mechanics, 242 (2021) 107426.

[53] Y. Tang, H. Chen, Characterization on crack propagation of nuclear graphite under three-point bending, Nuclear Materials and Energy, 20 (2019) 100687.

[54] Y. Tang, H. Chen, J. Xiao, Size effects on the characteristics of fracture process zone of plain concrete under three-point bending, Construction and Building Materials, 315 (2021) 125725.

[55] Y.S. Jenq, S.P. Shah, Two parameter fracture model for concrete, J Eng Mech, 111 (1985) 1227-1241.

[56] H. Chen, R.K.L. Su, A.S.-L. Fok, B. Yuan, An investigation of fracture properties and size effects of concrete using the ESPI technique, Magazine of Concrete Research, 72 (2020) 888-899.

[57] Y. Tang, H. Chen, Characterizations on fracture process zone of plain concrete, J Civ Eng Manag,

25 (2019) 819-830.

[58] Y.X. Tang, R.K.L. Su, H.N. Chen, Characterization on tensile behaviors of fracture process zone of nuclear graphite using a hybrid numerical and experimental approach, Carbon, 155 (2019) 531-544.

[59] Y. Tang, J. Xiao, H. Zhang, Z. Duan, B. Xia, Mechanical properties and uniaxial compressive stress-strain behavior of fully recycled aggregate concrete, Construction and Building Materials, 323 (2022) 126546.

[60] Y.X. Tang, J.Z. Xiao, D.C. Wang, M.Z. Zhang, Effect of carbonation treatment on fracture behavior of low-carbon mortar with recycled sand and recycled powder, Cement Concrete Comp, 142 (2023) 105178.

[61] H.H. Chen, R.K.L. Su, Tension softening curves of plain concrete, Construction and Building Materials, 44 (2013) 440-451.

[62] X. Hu, Q. Li, Z. Wu, S. Yang, Modelling fracture process zone width and length for quasi-brittle fracture of rock, concrete and ceramics, Engineering Fracture Mechanics, 259 (2022) 108158.

[63] S. Das, D. Stone, B. Mobasher, N. Neithalath, Strain energy and process zone based fracture characterization of a novel iron carbonate binding material, Engineering Fracture Mechanics, 156 (2016) 1-15.

[64] L. Skarzynski, J. Kozicki, J. Tejchman, Application of DIC Technique to Concrete-Study on Objectivity of Measured Surface Displacements, Exp Mech, 53 (2013) 1545-1559.

[65] A. Hillerborg, M. Modéer, P.E. Petersson, Analysis of crack formation and crack growth in concrete by means of fracture mechanics and finite elements Cement and Concrete Research, 6 (1976) 773-781

[66] RILEM, TC 50-FMC Fracture Mechanics of Concrete, Determination of the Fracture Energy of Mortar and Concrete by Means of Three-point Bend Tests on Notched Beams, Materials and Structures, 18 (1985) 287-290.

[67] R.K.L. Su, H.H.N. Chen, A.K.H. Kwan, Incremental displacement collocation method for the evaluation of tension softening curve of mortar, Engineering Fracture Mechanics, 88 (2012) 49-62.

[68] Y. Wu, T. Yin, Q. Li, D. Zhuang, Y. Chen, Z. Yang, Analytical investigation on the unstable fracture toughness of fine-grained quartz-diorite rock considering the size effect, Engineering

Fracture Mechanics, (2022) 108722.

[69] M. van den Heever, A. du Plessis, F. Bester, J. Kruger, G. van Zijl, A mechanistic evaluation relating microstructural morphology to a modified Mohr-Griffith compression-shear constitutive model for 3D printed concrete, Construction and Building Materials, 325 (2022) 126743.

[70] P. Nallathambi, B.L. Karihaloo, B.S. Heaton, Effect of Specimen and Crack Sizes, Water Cement Ratio and Coarse Aggregate Texture Upon Fracture-Toughness of Concrete, Magazine of Concrete Research, 36 (1984) 227-236.

[71] Y. Chen, Y. Zhang, Y. Xie, Z. Zhang, N. Banthia, Unraveling pore structure alternations in 3D-printed geopolymer concrete and corresponding impacts on macro-properties, Additive Manufacturing, 59 (2022) 103137.

[72] A. du Plessis, A.J. Babafemi, S.C. Paul, B. Panda, J.P. Tran, C. Broeckhoven, Biomimicry for 3D concrete printing: A review and perspective, Additive Manufacturing, 38 (2021) 101823.

[73] J.L. Liu, S. Li, K. Fox, P. Tran, 3D concrete printing of bioinspired Bouligand structure: A study on impact resistance, Additive Manufacturing, 50 (2022) 102544.

[74] J.H. Ye, K.Q. Yu, J.T. Yu, Q. Zhang, L.Z. Li, Designing ductile, tough, nacre-inspired concrete member in metric scale, Cement Concrete Comp, 118 (2021) 103987.